Applied Materials Today 48 (2026) 103071

Contents lists available at ScienceDirect

Applied Materials Today

journal homepage: www.elsevier.com/locate/apmt

Lunar regolith simulant-based triboelectric nanogenerators: Toward sustainable energy harvesting from resources on the moon

Alex Yohannan [a], Jayraj V. Vaghasiya [b], Keval K. Sonigara [a], Martin Pumera [a,c,d,e,*]

[a] Future Energy and Innovation Laboratory, Central European Institute of Technology, Brno University of Technology, Purkyňova 123, Brno 61200 Czech Republic
[b] School of Biomedical Engineering, Faculty of Engineering, The University of Sydney, NSW 2008, Australia
[c] Faculty of Electrical Engineering and Computer Science, VSB - Technical University of Ostrava, 17. listopadu 2172/15, 70800 Ostrava, Czech Republic
[d] Department of Medical Research, China Medical University Hospital, China Medical University, No. 91 Hsueh-Shih Road, Taichung 40402, Taiwan
[e] Department of Chemical and Biomolecular Engineering, Yonsei University, 50 Yonsei-ro, Seodaemun-gu, Seoul 03722, Korea

ARTICLE INFO

Keywords:
Space materials exploration
Energy generation
Sustainability
Moon regolith
Triboelectric generator

ABSTRACT

The exploration of extraterrestrial materials for energy harvesting, generation and storage is important for futuristic material evolution and use. Thus, study and use of extraterrestrial materials simulants becomes straightforward way to identify potential of those materials. Such as Lunar Regolith Simulants are tested as reference material to explore suitability for construction, solar cell components and beyond. However, aiming futuristic space exploration, on-site energy generator development from Lunar regolith materials is unexplored and necessary to unveil it. In this work, we introduce a lightweight, flexible triboelectric nanogenerator (TENG) that uses lunar regolith simulant particles (LRPs) embedded in polydimethoxysilane (PDMS) to harvest mechanical energy as first proof-of-concept. Under cyclic contact-separation, the optimized device containing 30 wt % of $\leq$ 45 μm LRPs yields an open-circuit voltage V_{oc} of ~10.5 V, a short-circuit current I_{sc} of ~2.2 μA, and a peak power density reached its maximum at 3.0 μW cm^{-2} under a force of 2.5 N at 10 Hz. Systematic optimization of grain size and weight fraction of LRPs in PDMS film is analyzed and resulted in the voltage output of 1.6 times and current density by 2.1 times compared to the bare PDMS material. Furthermore, the device shows 95 % performance retention of its output after 36,000 operation cycles, underscoring its good stability and potential for sustainable energy harvesting in ambient environments. These results demonstrate that utilizing extraterrestrial fillers, such as LRPs, is a useful approach for enhancing TENG performance in future terrestrial settings, offering insight for future space materials employed in composite design for TENG devices.

1. Introduction

Reliable and sustainable energy harvesting is essential for many small-scale applications like powering sensors, remote devices, and wearables [1–3]. TENG's have emerged as a promising technology for converting on-site mechanical energy into electricity due to their simple fabrication, low cost, and scalability [4]. The innovative device designs and materials diversity have attracted attention for enhancing triboelectric performance [5]. Their applications are not restricted to terrestrial materials; TENGs can also provide a useful model for studying energy-harvesting strategies in extraterrestrial contexts, such as lunar regolith exploration for energy application [6]. Establishing sustainable power sources on the lunar surface is crucial for long-term future missions like lunar bases and resource utilization [7]. Solar panels in space can efficiently power the equipment for basic needs due to their eco-friendly and economical approach [8,9], but their effectiveness is limited during long lunar nights [10,11]. This creates huge challenges for continuous energy and the need to develop an alternative sustainable energy source for future applications [11].

TENGs rely on the triboelectric effect, where charge transfer occurs between materials with different electron affinities during contact and separation. Since their first demonstration, TENGs have been widely explored in diverse scenarios, ranging from tiny-scale mechanical vibrations and human motion sensing to large-scale renewable sources [12–15]. The triboelectric properties, surface morphology, and dielectric characteristics of the materials used strongly influence the

* Corresponding author at: Future Energy and Innovation Laboratory, Central European Institute of Technology, Brno University of Technology, Purkyňova 123, Brno 61200 Czech Republic.
E-mail address: martin.pumera@ceitec.vutbr.cz (M. Pumera).

https://doi.org/10.1016/j.apmt.2025.103071
Received 31 July 2025; Received in revised form 4 November 2025; Accepted 22 December 2025
Available online 10 January 2026
2352-9407/© 2026 The Authors. Published by Elsevier Ltd. This is an open access article under the CC BY license (http://creativecommons.org/licenses/by/4.0/).

performance of a TENG [16]. While polymers like PDMS are widely employed as negative triboelectric materials, exploring alternative fillers can enhance performance and provide additional insights. Researchers have already shown promise by adding metal oxides like ZnO, TiO_2, and SiO_2 as fillers into the PDMS to enhance the triboelectric performance [6–9]. For instance, ZnO micro-balloon arrays have demonstrated impressive output performance, achieving an open-circuit voltage of approximately 57 V and a current density of 59 mA m^{-2} at a frequency of 100 Hz, which is significantly higher than that of devices without ZnO [17]. Similarly, TiO_2 nanotube arrays have been highlighted for their high surface area, which contributes to enhanced output power density and efficiency in TENG applications [18]. The mesoporous SiO_2 nanoparticles-based device exhibited a power density of 5.26 W m^{-2}, which is 25 times greater than pristine PDMS [19]. The incorporation of metal oxides not only improves the electrical output but also enhances the mechanical stability of TENGs, making them suitable for various applications, including wearable electronics and self-powered sensors [20–22].

LRPs are composed of fine-grained silicate minerals [23] and metal oxides, which inherently possess electronegative properties and high surface area, making them promising candidates as triboelectric fillers in composite TENG devices. Their unique chemical composition, particle shape, and surface characteristics may enhance charge generation and retention when embedded in a polymer matrix. By incorporating LRPs into PDMS, we can systematically study the effects of particle size, concentration, and dispersion on TENG performance. These LRPs contain approximately 75 % of Lunar Highlands (LHS-1) simulant and 25 % anorthosite agglutinates by weight. The addition of agglutinates increases the fidelity of LHS-1 in terms of glass composition, magnetic properties, and mechanical properties [24,25]. Studies have shown that the shape of LRPs significantly influences their mechanical properties, such as strength, packing density, and their interaction with spacecraft materials [26–28].

Importantly, using LRPs allows us to mimic lunar soil properties in a controlled platform to explore LRP-based TENGs. While the present study focuses on proof-of-concept experiments on Earth, the results also offer a quantitative framework for understanding how such materials might perform under extraterrestrial conditions, such as energy harvesting for lunar exploration missions. In this study, we developed a flexible and lightweight TENG device using a composite of LRPs and PDMS. To better understand the characteristics of the LRPs, we systematically studied their morphology, structure, and surface properties. We utilized four different particle sizes of LRPs, to examine their influence on the TENG's output performance. Also, optimized device performance by varying the concentration of LRPs in the composite. By tuning these parameters, we achieved a maximum output voltage of up to ~10.5 V, a peak current of ~2.2 μA. Furthermore, we demonstrated the device's ability to power small electronic components, establishing proof-of-concept for resource-driven energy harvesting with direct implications for future lunar surface missions.

2. Results and discussions

In this study, we developed a flexible TENG device using LRPs as the primary material for power generation applications. The schematic diagram (Fig. 1) represents the concept of utilizing LRPs in the

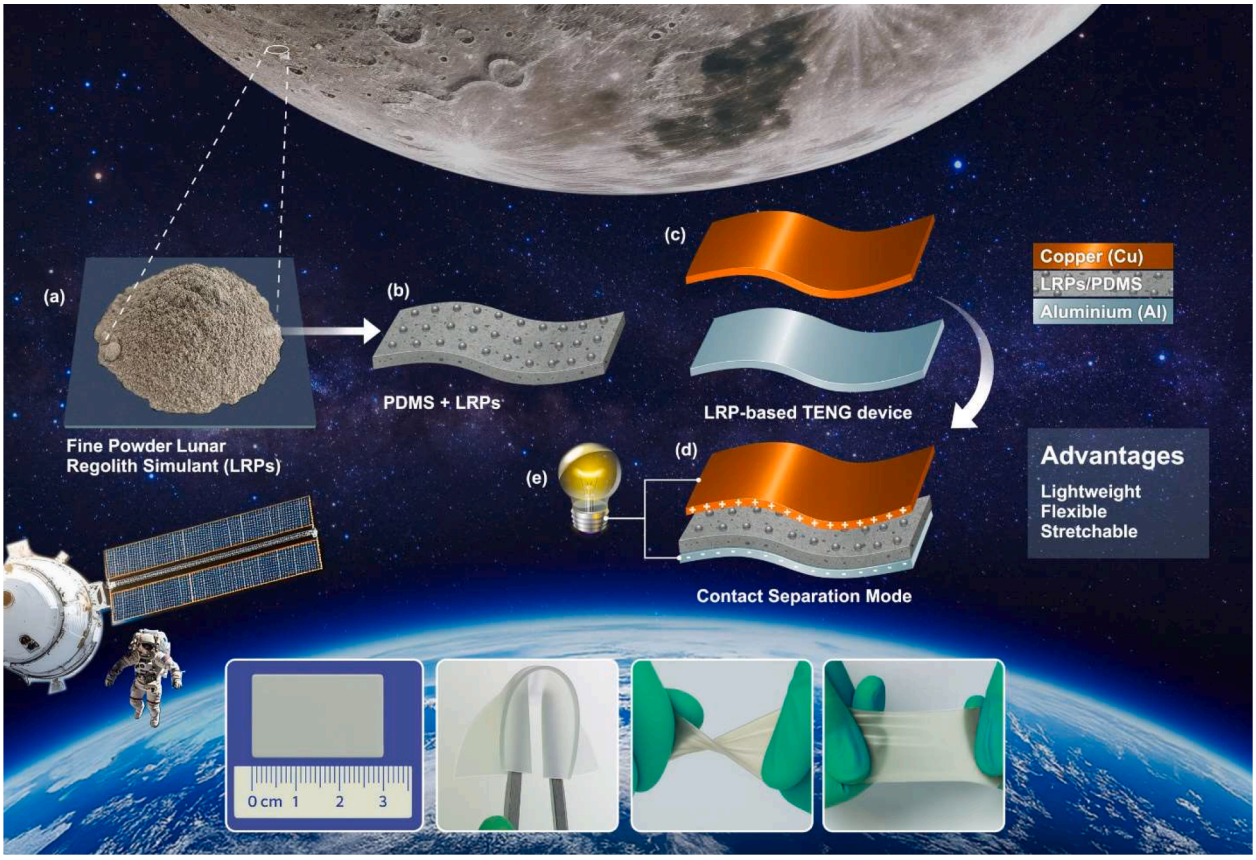

Fig. 1. Conceptual overview of the proposed work. Schematic illustration showing the design and operation of the TENG (a) Fine powdered commercial LRPs. (b) LRPs/PDMS composite triboelectric film serving as the active layer. (c) Cu and Al electrodes forming the top and bottom current collectors. (d) Assembly of the PDMS/LRPs composite film between the electrodes to construct the TENG prototype. (e) Contact–separation mode operation used to power a light-emitting diode (LED). The device demonstrates key advantages including small size, mechanical flexibility (bending, twisting and stretching), making it suitability for flexible electronic applications.

triboelectric electrode. As shown, LRPs were in the fine powdered form were embedded into a PDMS matrix to create a composite triboelectric layer (Fig. 1.a,b). The composite film was integrated with copper (Cu) and aluminum (Al) electrodes to construct the TENG device (Fig. 1.c,d). Upon periodic contact and separation of the layers, triboelectric charges are generated and electrostatically induced, resulting in alternating current flow between the electrodes. The generated charges are used to power small-scale electronics (Fig. 1.e). The LRPs–TENG exhibits desirable features such as lightweight construction, mechanical flexibility, and stretchability, offering a robust proof-of-concept for future self-powered systems in resource-constrained extraterrestrial environments (Fig. 1.f).

To achieve enhanced triboelectric properties, we prepared LRPs of various sizes and powder forms. The regolith simulant, initially in rock form, was first crushed into fine powder and then sieved into particle sizes of 250 μm, 125 μm, 63 μm, and 45 μm (see Figs. 2a–2d). These powdered LRPs were subsequently incorporated into PDMS to form the TENG structure. For more details, refer to the experimental and supplementary sections (**Supplementary Figure 1**) for the detailed sieving process and particle preparation. The potential difference between the positive and negative surface charges is responsible for TENG's power generation. Building on this foundation, incorporating PDMS into the LRPs enhances its performance as a superior negative triboelectric material. Al and Cu serve as positive triboelectric materials, strategically placed on the top and bottom sections and integrated with 3D-printed support for optimal functionality of electrodes. This design can increase its surface area and improve its charge retention capabilities.

Before exploring the performance study of the TENG device, it is essential to discuss the properties of the used LRP samples in this study and to understand their suitability for TENG devices. The surface morphology of the sample was analyzed using a scanning electron microscope (SEM) and energy-dispersive spectroscopy (EDS). The SEM images show that the sizes of the sieved LRPs fall within the expected ranges from 45 μm - 250 μm as shown in Figs. 2.e-h. The EDS analysis provides specific insights into the material compositions within the LRPs sample, such as oxygen, silicon, aluminum, silicon, magnesium, potassium, and iron, as shown in Fig. 2i, aligning with the known lunar soil compositions [29–31].

X-ray crystallography (XRD) was conducted to confirm these findings further and identify the simulant's crystalline structures (Fig. 3.a) [32]. The XRD patterns identify the presence of various oxides of silicate minerals content in higher amounts and the remaining elements present in nominal levels [33]. XRD-dominant planes, such as (100), (110), and (111), with prominent peaks observed at theta values of 21.2°, 31.6°, and 42.3°, respectively, indicate the presence of silica and other silicate-based minerals typical of lunar soil. The electronegative nature of the simulant is assessed using a zeta sizer, which measured a zeta potential of −17.47 mV (Figs. 3.b and 3.c). This negative charge is beneficial for the TENG applications as it enhances the material's ability to generate electrical energy through contact electrification. These

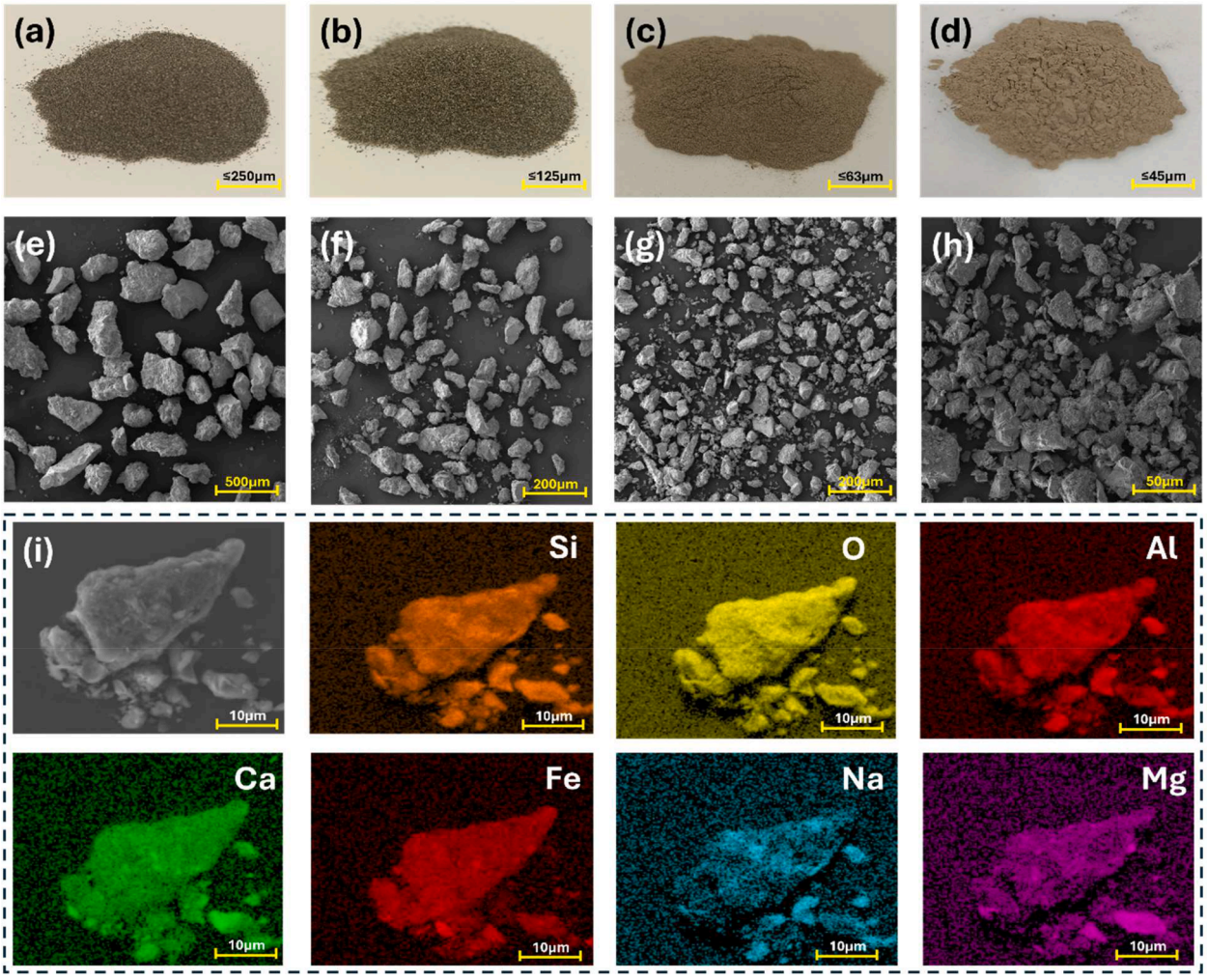

Fig. 2. Preparation of LRPs and morphology study. (a–d) Digital images of LRPs from 5 to 250 μm and (e–h) SEM images of LRPs as follows: (e) 250 μm, (f) 125 μm, (g) 63 μm, and (h) 45 μm. (i) EDS mapping of 45 μm LRPs.

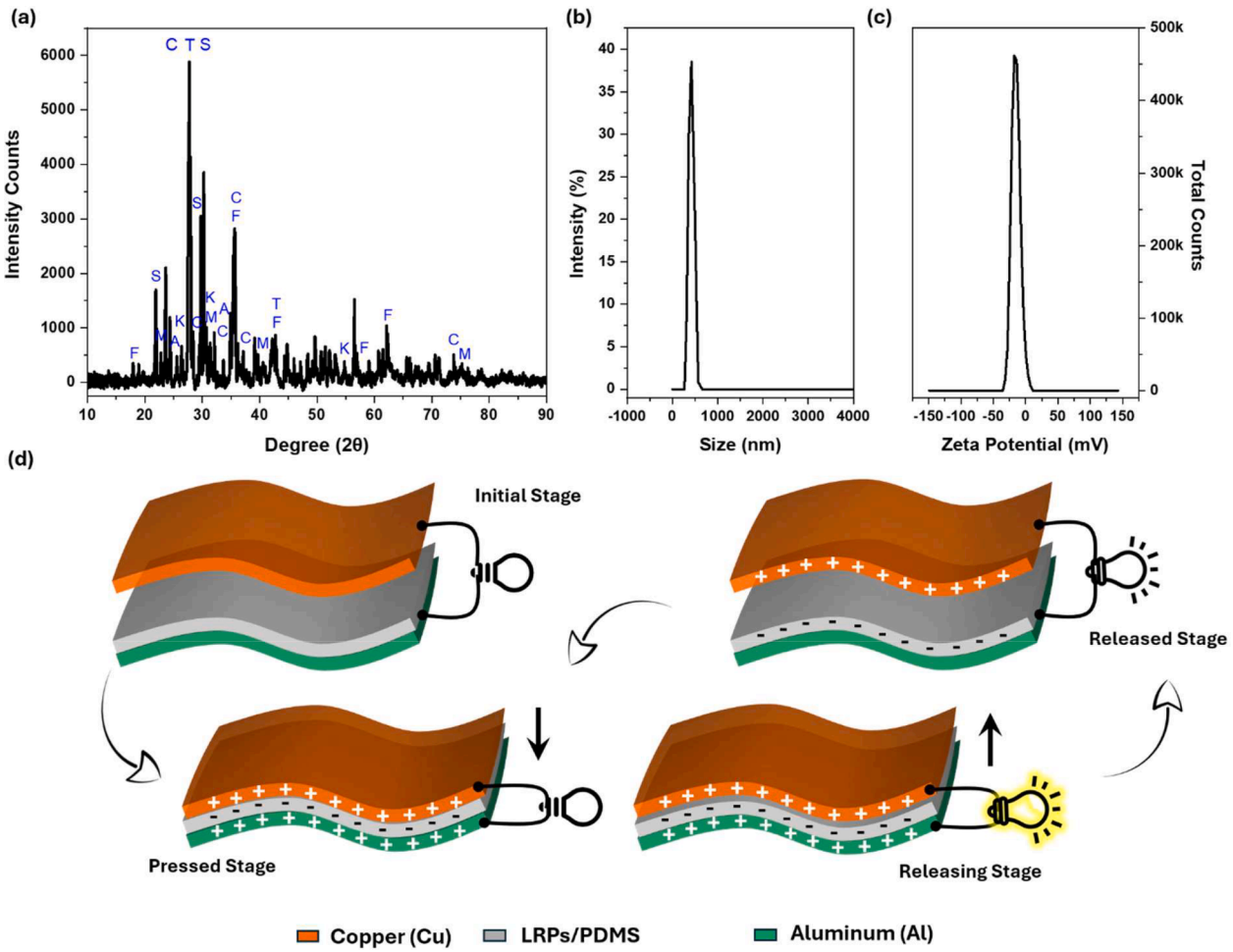

Fig. 3. Structural analysis and working principle of TENG device. (a) XRD spectra (where S, A, F, C, M, N, T, K denote probable oxide such as SiO_2, Al_2O_3, FeO, CaO, MgO, Na_2O, TiO_2, K_2O, respectively. (b) Size distribution analysis, (c) Zeta potential, and (d) schematic illustration of the TENG working mechanism.

results confirm its suitability for creating the TENG device using LRPs.

PDMS has the potential to generate negative triboelectric charges as a material [33]. Incorporating LRPs with an electronegative surface charge material can further improve TENG properties to develop a sustainable device. To fabricate this TENG device, LRPs of different grain sizes were intensively mixed with PDMS with a constant weight percent (wt %) of 10. The wt % of PDMS/LRPs composites are denoted as PDMS/LRPs-250, PDMS/LRPs-125, PDMS/LRPs-63, and PDMS/LRPs-45 in descending order, with decreasing grain sizes from big microparticles to fine nano-grain sizes.

The LRPs and PDMS mixture content was cast using the doctor blade method with the help of a customized 3D-printed template (15 mm (L) x 20 mm (W) x 0.15 mm (H)) designed by Autodesk Fusion 360 and sliced (Prusa-Slicer 2.4.2) with a layer thickness of 0.15 mm [34]. This is to achieve uniform thickness throughout the template. The optical microscopic images of the cured film samples are shown in **Supplementary Figure 2**. This is to ensure the dispersion level of PDMS/LRPs composition at each grain size. The PDMS/LRPs-45 shows a good distribution of LRPs in the prepared film.

A schematic representation showing the lateral view of constructed TENG devices with their different stages is presented in Fig. 3.d. The device's negative triboelectric layer (PDMS/LRPs) is placed between the aluminum foil and copper tape, which were utilized as current collectors. 3D-printed rectangle-faced polylactic acid (PLA) was used as the supporting substrate for the top and bottom layers. The easy construction of geometric shapes with polymeric materials within a minimal period of time allows this 3D printing technology for construction. According to the TENG structure shown in Fig. 3.d, the power generation mechanism *via* a linear damping system (actuator) hits the top plate of contact separation TENG device, making it possible for the regular contact separation between the electrodes and triboelectric layer. The triboelectric layer (PDMS/LRPs) is placed on the Cu tape, and the top current collector (Al foil) is separated by a polyurethane foam with a distance of 2 mm in height [34]. Initially, the whole device is stationary and remains neutral. Once the damping system starts hitting over the top layer, the Al foil comes in contact with the negative triboelectric layers of PDMS/LRPs, which create pressing and releasing movements throughout each cycle of the contact. During the pressing cycle, the PDMS/LRPs film contacts with Al foil and Cu tape placed at the top and bottom phases of the device, where the negative charges within the PDMS/LRPs film attract the positive charges and create a potential difference. In the next step, the entire system releases with the spring-back effect of polyurethane foam and the entire system becomes stable, leading to no charge transfer. Again, after this, the electrons move in the reverse direction, which generates an inverted signal peak. Thus, free electron movement occurs within the device as a result of an electrostatic induction effect, providing two output signals, open-circuit potential (V_{oc}) and short-circuit current (I_{sc}), through an oscilloscope.

Next, the output voltage and current of the fabricated TENGs were investigated. The output performance of PDMS/LRPs films was initially optimized by varying the grain sizes. The voltage output of PDMS/LRPs-250, PDMS/LRPs-125, PDMS/LRPs-63, and PDMS/LRPs-45 were studied at a contact frequency of 10 Hz and contact force of 2.5 N. For the initial study, we chose 10 wt. % of the LRPs sample with PDMS. The

performance is documented and plotted graphically in time (s) vs. voltage (V) in Fig. 4.a. It has been noted that the voltage output improves when the grain size becomes finer. The PDMS/LRPs-45 shows higher output than PDMS/LRPs-250. The average voltage output of PDMS/LRPs-45 is 7.5 ± 0.5 V; the peak-to-peak voltage is ≈ 8.0 V. Here, at finer grain sizes (≤ 45 μm and ≤ 63 μm), there is increased surface area and better interfacial contact, enhancing electron transfer and, thus, voltage output. Conversely, larger grain sizes (≤ 250 μm and ≤ 125 μm) reduce effective contact area, decreasing the voltage. The uneven dispersion of larger sizes in PDMS hinders effective surface contact and charge transfer, reducing voltage output. The improved performance of the PDMS/LRPs-45 composition film is attributed to the electronegative surface charges, where the particles are adequately dispersed altogether. The role of uniform dispersion in optimizing TENG performance is crucial. With these optimized results of grain size of PDMS/LRPs-45, we move further by varying the weight percent of LRPs (10, 30, 50, and 70 wt. %), called PDMS/LRPs-45@10 %, PDMS/LRPs-45@30 %, PDMS/LRPs-45@50 %, and PDMS/LRPs-45@70 %, respectively, as graphically represented in Fig. 4b It was found that the voltage output of the 30 wt. % sample (PDMS/LRPs-45@30 %) exhibited better results, averaging 8.0 ± 0.5 V with peak-to-peak voltage ≈10.5 V. With respect to the voltage output, the short-circuit current output results also followed the same trend where the 30wt % sample shows the highest output of ~2.2 μA as plotted in Fig. 4.c. Here, optimal contact and charge transfer likely occurred, leading to the highest voltage output of ~10.5 V and current output of ~2.2 μA. Deviations from this weight percent may disrupt this balance, resulting in lower voltage outputs due to excessive regolith simulant content. Higher concentrations of regolith (70 %) and excessive particle loading can lead to overcrowding within the PDMS matrix, reducing voltage output by ~5 V at PDMS/LRPs-45@70 % composition and demonstrating the reduction of effective surface contact and interfacial interactions necessary for efficient charge transfer. To easily understand the comparison of various LRPs sizes and weight percent voltage output shown in Fig. 4d, we have chosen the optimized film (PDMS/LRPs-45@30 %) for further analysis in the upcoming sections.

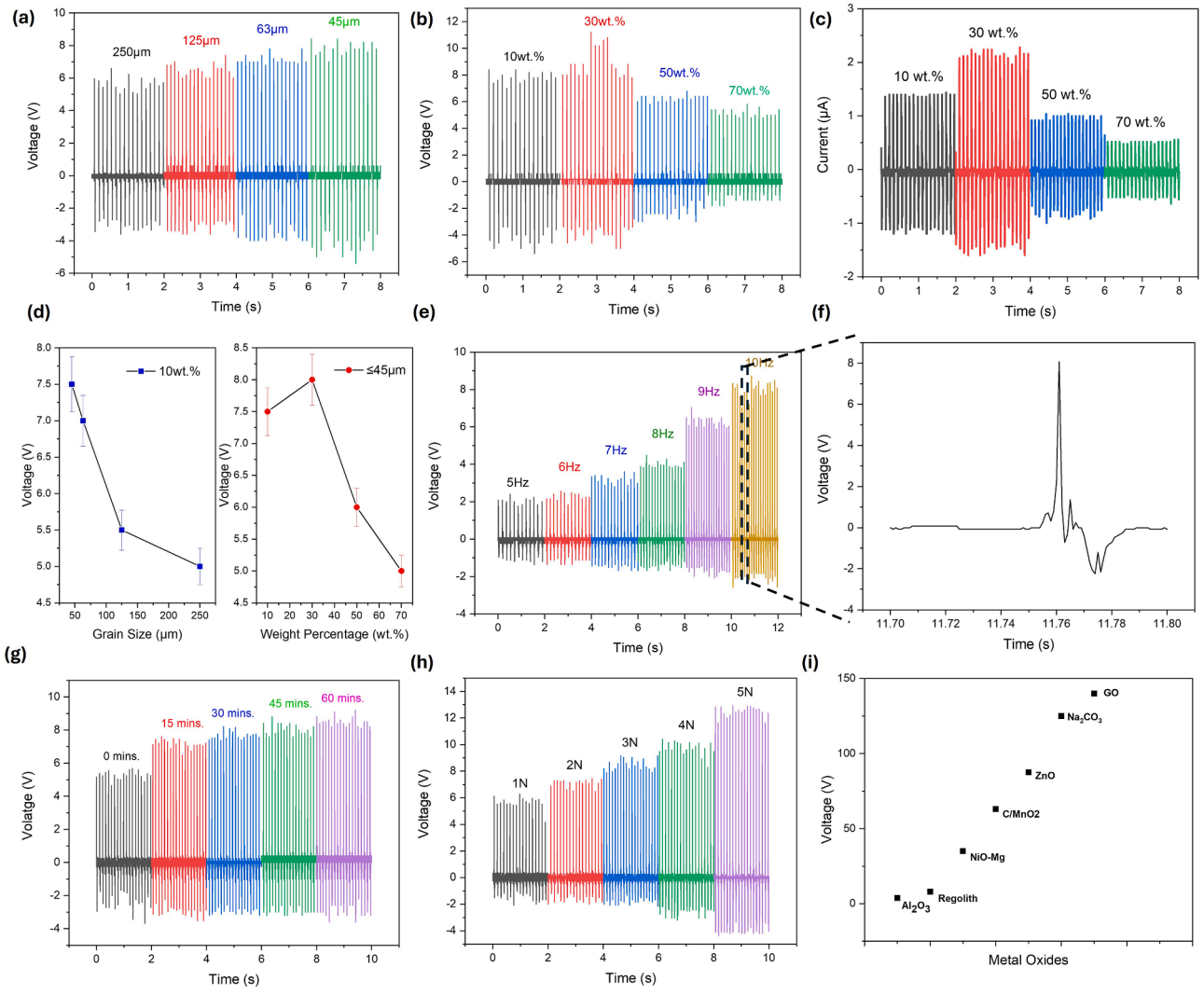

Fig. 4. Optimization of TENG performance. (a) variation different LRPs sizes (250, 125, 63, 45 μm as PDMS/LRPs-250, PDMS/LRPs-125, PDMS/LRPs-63, and PDMS/LRPs-45) with constant 10 wt % concentration. (b, c) voltage and current output of PDMS/LRPs-45 sample at different wt % composition (10, 30, 50, 70 wt % as PDMS/LRPs-45@10 %, PDMS/LRPs-45@30 %, PDMS/LRPs-45@50 %, and PDMS/LRPs-45@70 %). (d) Comparison of output voltage across samples with varying grain sizes (250 - 45 μm) at a fixed filler loading of 10 wt %, and voltage comparison for different composite compositions (wt %) using the optimized grain size of 45 μm is also shown. Error bars represent the standard deviation from multiple measurements. (e) Voltage output as a function of frequency. (f) Magnified plots of voltage against time of optimized sample with 10 Hz frequency level. (g) Number of cycles with respect to the time moves, with freshly prepared sample measured from the start up to 60 min. (h) Voltage output upon varying forces. (i) Measurements taken from the literature on voltage output of different metal oxide materials with PDMS.

Minor variations in the output of the optimized regolith simulant film sample (PDMS/LRPs-45@30 %) were found during pressing and releasing cycles, and for a long time period of damping. These changes were systematically investigated to assess their durability and performance stability. Initially, we studied the role of damping frequency influencing the voltage output. The film sample was subjected to frequencies ranging from 5 to 10 Hz. It was observed that the output voltage varied correspondingly with the change in frequency, with the maximum output being recorded at 10 Hz as shown in Fig. 4.e. An enlarged view of the signal from Fig. 4.e was analyzed to interpret the device's mechanism further. The graph clearly demonstrates the presence of positive and negative peaks, corresponding to the pressing and releasing cycles of the device, respectively, indicating the functionality of the TENG mechanism (Fig. 4.f).

Thus, the observed asymmetry in the potential differences between the electrodes during the cycles can be attributed to several factors. These factors include contact electrification, electrostatic induction, and charge redistribution between the electrodes [32]. These effects contribute to the varying intensities of the alternating signals. The movement of the top plate with respect to the speed of the damping device directly affects the output performance of the device. As shown in Fig. 4.e, the output voltage increases consistently as the speed of the hitting layer increases. The magnified signals of voltage output are emphasized in the form of a sinusoidal waveform with respect to the pressing and releasing cycles. Then, the durability of the sample was studied using a freshly prepared optimized composition sample (PDMS/LRPs-45@30 %), which exhibited an output voltage of approximately 6 V during the very beginning stage. However, after 15 min of continuous operation, the output voltage increased to ~8.5 ± 0.2 V. Subsequent measurements were recorded at 15-minute intervals, revealing minor fluctuations in the output voltage of ± 0.1 V over a duration of 60 min, and this period corresponded to nearly 36,000 cycles of the damping system as illustrated in Fig. 4.g. Then, in Fig. 4.h, the impact of the varying forces on the TENG device is depicted by maintaining a constant frequency (10 Hz). The results show that the output voltage density increases with the rise in external force. Specifically, the output voltage reaches ~12.5 ± 0.5 V when an external force of 5 N is applied. It is evident that external force significantly impacts the output performance compared to the other parameters. When a higher external force is applied, the materials compress more, increasing contact area and generating more electrons, thereby greatly enhancing the TENG's output performance. This study proves the device's performance will significantly improve with increasing the external forces.

There are a few reports of metal oxide-based TENG devices and their performance is compared with our regolith-based TENG device in Fig. 4. i. Notably, the Al_2O_3-based TENG shows a lower output than our device, whereas some devices based on C/MnO_2 [35] and Na_2Co_2 [36] exhibit higher performance. Aneeta *et al.* [37] synthesized a TENG device using a NiO-Mg magnetic nanocomposite, which exhibited an impressive output of 35 V. Zhang *et al.* [35] introduced a TENG with a porous C/MnO_2 nanocomposite structure, yielding an output of 63 V. Sedeh *et al.* [38] showcased a high-performance single-electrode TENG (SE-TENG) on a PDMS surface modified with ZnO nanotubes, achieving an output of 87.5 V. These studies demonstrate that diverse approaches to metal oxides with PDMS can enhance the efficiency of TENG devices. In a similar way, LRPs comprising metal oxides can enhance TENG output with the incorporation in PDMS. This comparison highlights the potential of lunar regolith as an effective triboelectric material, especially in future space applications. To further quantify the device performance, the power output characteristics of the optimized TENG device were systematically evaluated (**Supplementary Figure 03**). By tuning the external load resistance between 1 Ω and 10^7 Ω, the voltage output exhibited a monotonic increase, while the current density decreased in accordance with Ohm's law. The maximum power density of the device was achieved at 3.0 μW cm^{-2} with an external resistance of 8.2 × 10^5 Ω, demonstrating that careful adjustment of both filler composition and load matching can significantly enhance the efficiency of TENG devices.

To contextualize the performance of our LRPs/PDMS TENG relative to existing PDMS-based TENGs incorporating metal oxides, we compiled representative literature data in **Supplementary Table 01**. While several metal oxide-based TENGs exhibit higher Voc and Isc, these studies often involve larger device areas or complex nanostructures. When normalized for device area and expressed in terms of power density, our optimized LRPs/PDMS TENG achieves 3.0 μW cm^{-2}, which is comparable with or exceeds several previously reported devices under similar laboratory-scale dimensions (**Supplementary Table 01**). Notably, the LRPs/PDMS device demonstrates a better short-circuit current of 2.5 μA, which is on par with or exceeds some metal oxide composites of similar size, despite the relatively simple fabrication and the use of naturally occurring lunar regolith simulants. This proof-of-concept demonstration on Earth confirms that lunar regolith particles can serve as effective triboelectric materials in flexible and lightweight TENGs. Importantly, this study establishes a baseline for future investigations into cost-effective, scalable, and environmentally benign TENG designs, offering a promising direction for both terrestrial energy-harvesting applications and potential adaptation for lunar surface energy systems.

The practical application phase of this study involved conducting a series of mechanical and electrical tests on the optimized sample. In Figs. 5a–5e, a ruler was initially used to confirm that the sample length was 30 mm. The sample then underwent rigorous mechanical tests, including bending, twisting, and stretching, which were all successful. Subsequently, the sample was weighed using a microbalance. With the PLA substrate, the total weight was 9 g When the sample was measured without the PLA substrate, including only the current collectors and the film, the weight was reduced to approximately 1.5 g This significant reduction in weight highlights the sample's potential for lightweight applications.

In practical testing, the voltage output of the optimized sample was evaluated using a finger-tapping mechanism. During normal tapping, the sample produced an average voltage of ~ 12 ± 2.5 V (Fig. 5.f). In contrast, vigorous tapping resulted in a substantial increase, with the voltage reaching up to ≈ 30 ± 5.0 V (Fig. 5.g). These results suggest the sample's high sensitivity to mechanical stimuli. This involved mechanical movement simulations like meteor showers. Thus, stone pieces of similar weight (≈ 300 g) were showered onto the device, yielding a voltage output of approximately ≈ 10.5 V (Fig. 5h). When stone pieces of varying weights (≈ 200gm - 600gms) were used, the power output surged to ~ 27 ± 1.5 V (Fig. 5i), demonstrating the sample's robust response to diverse mechanical impacts. The AC signals generated were rectified to DC signals using a bridge rectifier connected to the TENG output terminals. The rectified DC voltage is presented in Fig. 6.c. The experimental setup of the bridge rectifier setup is shown in Fig. 6.a. Notably, this configuration enabled the direct powering of light emitting diode as shown in Fig. 6.b, with additional footage provided in Supplementary **Movie 1**.

Based on these findings, it can be concluded that the optimized sample has strong potential for lightweight, better-performance applications in environments subject to varying mechanical stimuli, such as the lunar surface. The significant voltage outputs and successful rectification demonstrate its feasibility for practical energy harvesting and other related applications. Moreover, the durability and frequency response of the optimized regolith simulant film sample were thoroughly evaluated, demonstrating significant insights into the TENG device's performance characteristics and underlying mechanisms.

3. Conclusion

In this work, feasibility and functionality of LRPs is studied and demonstrated as dopant in PDMS triboelectric film for improved TENG devices to harvest mechanical energy into electrical energy. The

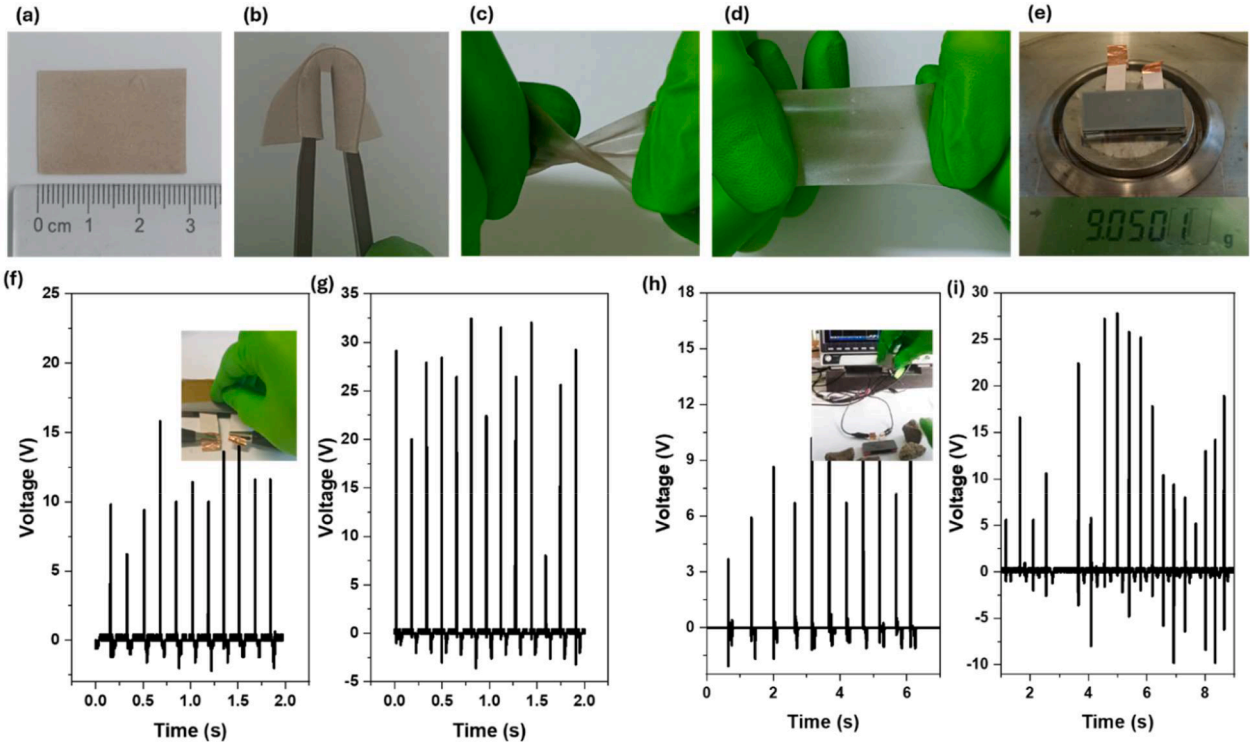

Fig. 5. Flexibility and robustness study of TENG. (a–d) PDMS/LRPs45@30 % film flexibility study by bending, twisting, and stretching. (e) Weight of the whole device. Variation in voltage against time while tapping (f) normally and (g) vigorously. Stone showering in (h) similar weight and (i) different weighted stones.

optimized device shows maximum V_{oc} of ~10.5 V, I_{sc} of ~2.2 μA, and a maximum power density of 3.0 μW cm^{-2} under 10 Hz, 2.5 N mechanical excitation, with LRPs of ≤ 45 μm grain size with 30 wt % composition. Here it is concluded that the grain size of LRPs and loading effectively stimulates TENG performance and these are key factors to achieve higher power from the device. The TENG devices show long-term stability and robust mechanical properties, when exposed to rigorous test of stone shower induced energy generation. It could be extended to flexible wearable application due to excellent flexibility and stretchability, that could inspire on-site energy generators for astronauts to power sensors. As, TENG device successfully power light-emitting diode as real demonstration. Further, LRPs can be utilized in TENG devices with different aspects to tune the strength of films as filler, modulate polarity, dielectric property or could be use as standalone triboelectric materials if cast in solid film. We believe that our study will inspire future technological advancements in the design of energy systems for long-duration lunar missions and beyond. To further identify the feasibility of these TENGs, testing in simulated space or lunar environmental conditions is important.

4. Experimental section

Materials: The SYLGARD 184 silicone elastomer kit was obtained from Dow, USA. The PLA filaments for 3D printing were sourced from Filament2Print, Spain. Sieve Stacks for regolith sieving were procured from Retsch, Verder Scientific, Germany. LRPs were obtained from Space Resource Technologies (SRT), UCF's Exolith Lab, Florida, composition according to company analysis with 75 % LHS-1 Lunar Highlands Simulant and 25 % Anorthosite Agglutinates, by wt.

Preparation of PDMS/LRPs film: The experimental study starts with fabricating the PDMS film. The silicone elastomer solution and curing agent were mixed in a mass ratio of 10:1 to fabricate the film. The experiment began with a 10 wt. % LR sample of varying grain sizes. The LR sample was sieved using a Sieve shaker (Retsch) and collected into four different grain sizes as follows (250, 125, 63, and 45 μm). The powdered sieved LRPs were mixed with the elastomer solution and stirred for 15 min. Subsequently, we added the curing agent and stirred it for 10 min as per the required ratio mentioned above. The PDMS/LRPs mixture was kept in a vacuum for 2 h for degassing. Then, the mixture was poured into a Petri dish containing a 3D-printed PLA mold (L x B: 20 mm x 30 mm) with a thickness of 0.15 mm to achieve uniform thickness and follow the doctor's blade technique. The mixture was then ready to be placed in an electric oven set at 80 °C for 1.5 h to finish the curing process. The low temperature curing process of the mixture was carefully chosen to ensure that the PLA mold would not experience distortion. After the preferred time, the petri dish containing the films was kept at room temperature for 4 h. Then, the PDMS/LRP films were carefully peeled away from the 3D mold. The same procedure was followed for preparing the PDMS/LRPs mixture for varying weight percent levels as follows (PDMS/LRPs-45@10 %, PDMS/LRPs-45@30 %, PDMS/LRPs-45@50 %, and PDMS/LRPs-45@70 %). A PDMS film was created following the same process, but without adding LRPs for fabrication of the control device.

In this study, we selected PDMS casting as the primary method for fabricating LRPs–based triboelectric layers because it offers simplicity, reproducibility, and suitability for proof-of-concept validation. We note, however, that other approaches such as solution casting, printing, electrospinning, and surface modification are also feasible and could broaden the performance and design space. For clarity, we summarize these methods, along with their respective advantages and limitations, in **Supplementary Table 02**.

Fabrication of TENG: The PDMS/LRPs film (20 mm × 30 mm) was placed on a sheet of Al foil of the same size (thickness 25 μm) with the PDMS/LRPs film surface facing upwards. A conductive Cu adhesive tape was attached to the Al foil to connect it to the oscilloscope probe terminal. The Al foil was placed on a 3D-printed PLA substrate patterned in square patterns with minimal distance to achieve a rough surface as the bottom plate. The PDMS/LRPs was placed onto the surface of the Al-based layer. Similarly, the top plate was also designed with the same pattern as PLA substrate and was attached parallel to each other with

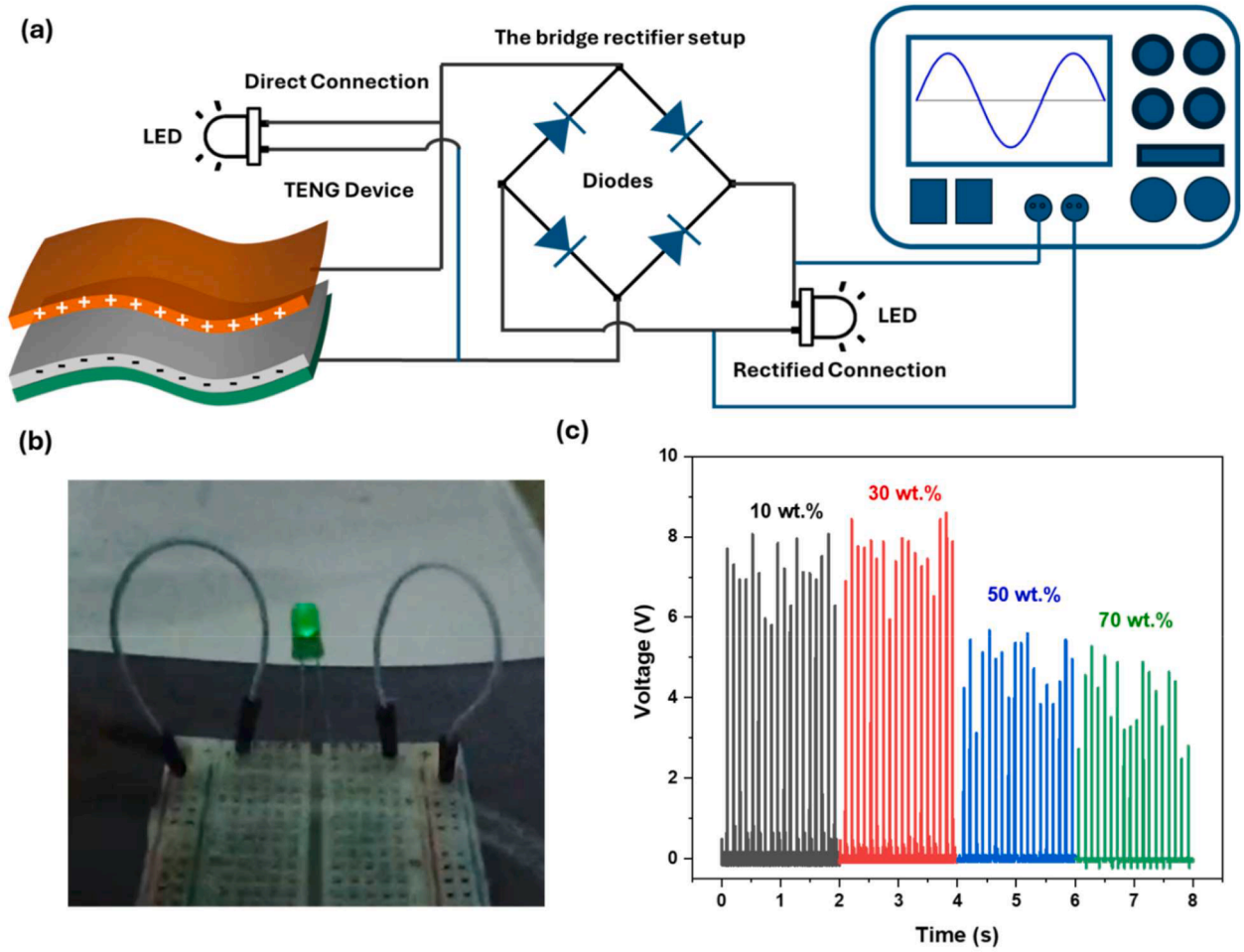

Fig. 6. Schematic representation of the experimental setup. (a) Connection of the TENG device with bridge rectifier through an LED and direct connection of LED from the TENG device, and oscilloscope output of TENG device. (b) Photograph of LED glowing with the TENG direct circuit. (c) Variation of rectified voltage at different weight percent while connected by a bridge rectifier with the TENG terminals (contact force is 2.5 N).

copper tape instead of Al foil paper. The top and bottom plates were carefully connected with polyurethane foam spacers placed in between the PLA plates on both sides of the device. It is important to note that the spacers maintain a specific distance of 2–3 mm between the triboelectric layers to ensure optimal performance.

Characterization: To characterize the surface morphology and composition of LRPs in detail, scanning electron microscope (SEM) analyses were performed with MIRA3 XMU (MIRA-STAN) while elemental composition was confirmed using energy-dispersive X-ray spectroscopy (EDS) on the EDS detector (Oxford Instruments X-MAX20). The crystallographic structure was analyzed by X-ray diffraction (XRD) using the Rigaku SmartLab 3 kW powder diffractometer with Brag Brentano geometry and a Cu K*a* radiation source. Size distribution and Zeta potential were measured using the Malvern Panalytical Zetasizer Ultra, with the cuvette positioned inside the instrument. All measurements conducted in Zeta potential were run three times to obtain error bars.

Electrical Measurement: Electrical measurements for this device were recorded using a digital oscilloscope (GW Instek GDS-1074B). An electric linear motor actuator, called the damping system, with a hub measured to be 25 mm in length (24 V DC, max 1000 rpm, DAOE) was used to tap on the contact separation TENG device. This creates a periodic contact release action between the tip of the actuator and the top plate of the TENG device, having frequencies varying from 10 to 50 Hz. A crocodile connector was used to connect the two tips of the oscilloscope probe to the Cu strips of the triboelectric layer and electrodes on both plates.

CRediT authorship contribution statement

Alex Yohannan: Conceptualization, Methodology, Investigation, Validation, Visualization, Project administration, Writing – original draft. **Jayraj V. Vaghasiya:** Methodology, Writing – review & editing, Supervision. **Keval K. Sonigara:** Methodology, Writing – review & editing, Supervision. **Martin Pumera:** Conceptualization, Writing – review & editing, Supervision, Project administration, Funding acquisition, Conceptualization.

Declaration of competing interest

Authors declare no conflict of interests.

Acknowledgements

The work was supported by the ERDF/ESF project TECHSCALE (No. CZ.02.01.01/00/22_008/0004587). This research was co-funded by the European Union under the REFRESH – Research Excellence for Region Sustainability and High-tech Industries project number CZ.10.03.01/00/22_003/0000048 *via* the Operational Programme Just Transition. CzechNanoLab project LM2023051 funded by MEYS CR is gratefully acknowledged for the financial support of the measurements/sample fabrication at CEITEC Nano Research Infrastructure.

Supplementary materials

Supplementary material associated with this article can be found, in the online version, at doi:10.1016/j.apmt.2025.103071.

Data availability

Data will be made available on request.

References

[1] Q. Ullah, T. Rauta, J. Keskikuru, J. Haverinen, P. Ruuskanen, Innovations in energy harvesting: a survey of low-power technologies and their potential, Energy Rep. 14 (2025) 671–692, https://doi.org/10.1016/j.egyr.2025.06.019.

[2] A. Ali, H. Shaukat, H. Elahi, S. Taimur, M.Q. Manan, W.A. Altabey, S.A. Kouritem, M. Noori, Advancements in energy harvesting techniques for sustainable IoT devices, Results Eng. 26 (2025) 104820, https://doi.org/10.1016/j.rineng.2025.104820.

[3] Z. Gao, Y. Zhou, J. Zhang, J. Foroughi, S. Peng, R.H. Baughman, Z.L. Wang, C. H. Wang, Advanced energy harvesters and energy storage for powering wearable and implantable medical devices, Adv. Mater. 36 (2024) 2404492, https://doi.org/10.1002/adma.202404492.

[4] T. Cheng, J. Shao, Z.L. Wang, Triboelectric nanogenerators, Nat. Rev. Methods Primers 3 (2023) 39, https://doi.org/10.1038/s43586-023-00220-3.

[5] C. Wang, H. Guo, P. Wang, J. Li, Y. Sun, D. Zhang, An advanced strategy to enhance TENG output: reducing triboelectric charge decay, Adv. Mater. 35 (2023) 2209895, https://doi.org/10.1002/adma.202209895.

[6] S. Gao, T. Ma, N. Zhou, J. Feng, P. Huayan, J. Luo, P. Pennacchi, F. Chu, Q. Han, Extremely compact and lightweight triboelectric nanogenerator for spacecraft flywheel system health monitoring, Nano Energy 122 (2024) 109330, https://doi.org/10.1016/j.nanoen.2024.109330.

[7] NASA, NASA outlines lunar surface sustainability concept, NASA (2020). https://www.nasa.gov/news-release/nasa-outlines-lunar-surface-sustainability-concept.

[8] NASA, NASA's lunar exploration program overview, NASA Technical Report (2020). https://ntrs.nasa.gov/citations/20205001338.

[9] A.A.F. Husain, W.Z.W. Hasan, S. Shafie, M.N. Hamidon, S.S. Pandey, A review of transparent solar photovoltaic technologies, Renew. Sustain. Energy Rev. 94 (2018) 779–791, https://doi.org/10.1016/j.rser.2018.06.031.

[10] A. Bermudez-Garcia, P. Voarino, O. Raccurt, Environments, needs and opportunities for future space photovoltaic power generation: a review, Appl. Energy 290 (2021) 116757, https://doi.org/10.1016/j.apenergy.2021.116757.

[11] R. Verduci, V. Romano, G. Brunetti, N. Yaghoobi Nia, A. Di Carlo, G. D'Angelo, C. Ciminelli, Solar energy in space applications: review and technology perspectives, Adv. Energy Mater. 12 (2022) 2200125, https://doi.org/10.1002/aenm.202200125.

[12] R. Gu, L. Wei, N. Xu, Y. Xiong, Q. Sun, Z.L. Wang, Machine learning enhanced self-charging power sources, Adv. Funct. Mater. 35 (2025) 2505719, https://doi.org/10.1002/adfm.202505719.

[13] C. Xu, J. Yu, Z. Huo, Y. Wang, Q. Sun, Z.L. Wang, Pursuing the tribovoltaic effect for direct-current triboelectric nanogenerators, Energy Environ. Sci. 16 (2023) 983–1006, https://doi.org/10.1039/D2EE04019K.

[14] W. Tang, Q. Sun, Z.L. Wang, Self-powered sensing in wearable electronics: a paradigm shift technology, Chem. Rev. 123 (2023) 12105–12134, https://doi.org/10.1021/acs.chemrev.3c00305.

[15] S. Mappoli, K.K. Sonigara, R. Nittoor-Veedu, M. Pumera, MAX phase metal carbide-enabled triboelectric nanogenerator for integrated ammonia generation, Appl. Mater. Today 47 (2025) 102919, https://doi.org/10.1016/j.apmt.2025.102919.

[16] A. Mohapatra, N. Divakaran, A. Y, A.K. PV, S. Mohanty, The significant role of CNT–ZnO core–shell nanostructures in the development of FDM-based 3D-printed triboelectric nanogenerators, Mater. Today Nano 22 (2023) 100313, https://doi.org/10.1016/j.mtnano.2023.100313.

[17] W. Deng, B. Zhang, L. Jin, Y. Chen, W. Chu, H. Zhang, M. Zhu, W. Yang, Enhanced performance of ZnO microballoon arrays for a triboelectric nanogenerator, Nanotechnology 28 (2017) 185402, https://doi.org/10.1088/1361-6528/aa5f34.

[18] R. Mohammadpour, Flexible triboelectric nanogenerator based on high surface area TiO_2 nanotube arrays, Adv. Eng. Mater. 20 (2018) 1700767, https://doi.org/10.1002/adem.201700767.

[19] W. Li, Y. Xiang, W. Zhang, K. Loos, Y. Pei, Ordered mesoporous SiO_2 nanoparticles as charge storage sites for enhanced triboelectric nanogenerators, Nano Energy 113 (2023) 108539, https://doi.org/10.1016/j.nanoen.2023.108539.

[20] Y. Yang, N. Sun, Z. Wen, P. Cheng, H. Zheng, H. Shao, Y. Xia, C. Chen, H. Lan, X. Xie, C. Zhou, J. Zhong, X. Sun, S.T. Lee, Liquid-metal-based super-stretchable and structure-designable triboelectric nanogenerator for wearable electronics, ACS Nano 12 (2018) 4666–4674, https://doi.org/10.1021/acsnano.8b00147.

[21] D. Lu, T. Liu, X. Meng, B. Luo, J. Yuan, Y. Liu, S. Zhang, C. Cai, C. Gao, J. Wang, S. Wang, S. Nie, Wearable triboelectric visual sensors for tactile perception, Adv. Mater. 35 (2023) 2209117, https://doi.org/10.1002/adma.202209117.

[22] Y. Liu, J. Wang, T. Liu, Z. Wei, B. Luo, M. Chi, S. Zhang, C. Cai, C. Gao, T. Zhao, S. Wang, S. Nie, Triboelectric tactile sensor for pressure and temperature sensing in high-temperature applications, Nat. Commun. 16 (2025) 383, https://doi.org/10.1038/s41467-024-55771-0.

[23] A. Ellery, Sustainable in-situ resource utilization on the moon, Planet. Space Sci. 184 (2020) 104870, https://doi.org/10.1016/j.pss.2020.104870.

[24] J. Patzwald, R. Kleba-Ehrhardt, F. Schiperski, T. Griemsmann, S. Linke, T. Neumann, L. Overmeyer, E. Stoll, D. Karl, Properties of novel LX lunar regolith simulant system — The base simulants: part 1, Acta Astronaut 231 (2025) 200–222, https://doi.org/10.1016/j.actaastro.2025.02.030.

[25] J. Long-Fox, M.P. Lucas, Z. Landsman, C. Millwater, D. Britt, C. Neal, Applicability of Simulants in Developing Lunar Systems and infrastructure: Geotechnical measurements of Lunar Highlands Simulant LHS-1, in: Earth and Space 2022, American Society of Civil Engineers, Reston, VA, 2023, pp. 76–85, https://doi.org/10.1061/9780784484470.007.

[26] D. Rickman, C. Immer, P. Metzger, E. Dixon, M. Pendleton, J. Edmunson, Particle shape in simulants of the lunar regolith, J. Sediment. Res. 82 (2012) 822–828, https://doi.org/10.2110/jsr.2012.69.

[27] M.B. Duke, L.R. Gaddis, G.J. Taylor, H.H. Schmitt, Development of the moon, Rev. Mineral. Geochem. 60 (2006) 597–654, https://doi.org/10.2138/rmg.2006.60.6.

[28] I.A. Crawford, Lunar resources: a review, Prog. Phys. Geogr. 39 (2015) 137–167, https://doi.org/10.1177/0309133314567585.

[29] E.N. Slyuta, Physical and mechanical properties of the lunar soil (a review), Sol. Syst. Res. 48 (2014) 330–353, https://doi.org/10.1134/S0038094614050050.

[30] E.N. Slyuta, Physical and mechanical properties of the lunar soil (a review), Sol. Syst. Res. 48 (2014) 330–353, https://doi.org/10.1134/S0038094614050050.

[31] A.A. Altun, F. Ertl, M. Marechal, A. Makaya, A. Sgambati, M. Schwentenwein, Additive manufacturing of lunar regolith structures, Open Ceram. 5 (2021) 100058. 10.1016/j.oceram.2021.100058.

[32] Q. Ma, H. Wang, Analysis of the direct shear test and microstructure of the lunar soil simulant solidified by sodium silicate, Adv. Mater. Sci. *Eng.* 2022 (2022) 7654781, https://doi.org/10.1155/2022/7654781.

[33] T. Xu, J. Ye, J. Tan, Unravelling the ageing effects of PDMS-based triboelectric nanogenerators, *Adv.* Mater. Interfaces 11 (2024) 2400094, https://doi.org/10.1002/admi.202400094.

[34] K. Ghosh, C. Iffelsberger, M. Konečný, J. Vyskočil, J. Michalička, M. Pumera, Nanoarchitectonics of triboelectric nanogenerator for conversion of abundant mechanical energy to green hydrogen, Adv. Energy Mater. 13 (2023) 2203476, https://doi.org/10.1002/aenm.202203476.

[35] H. Zhang, P. Zhang, P. Li, L. Deng, W. Zhang, B. Liu, Z. Yang, Enhanced performance triboelectric nanogenerator based on porous structure C/MnO_2 nanocomposite for energy harvesting, Nano Res. 15 (2022) 10406–10414, https://doi.org/10.1007/s12274-022-4326-2.

[36] C. Cui, X. Wang, Z. Yi, B. Yang, X. Wang, X. Chen, J. Liu, C. Yang, Flexible single-electrode triboelectric nanogenerator and body moving sensor based on porous na_2co_3/polydimethylsiloxane film, ACS Appl. Mater. Interfaces 10 (2018) 3652–3659, https://doi.org/10.1021/acsami.7b17585.

[37] A.M. Padhan, S. Hajra, S. Nayak, J. Kumar, M. Sahu, H.J. Kim, P. Alagarsamy, Triboelectrification based on NiO–Mg magnetic nanocomposite: synthesis, device fabrication, and energy harvesting performance, Nano Energy 91 (2022) 106662, https://doi.org/10.1016/j.nanoen.2021.106662.

[38] A. Dorri Sedeh, F. Karimzadeh, M. Kharaziha, A high-performance single-electrode triboelectric nanogenerator based on polydimethylsiloxane surface modified using zinc oxide nanotubes: fabrication and simulation, Sustain. Energy Technol. Assess 56 (2023) 103058, https://doi.org/10.1016/j.seta.2023.103058.